Research Square

Preprints are preliminary reports that have not undergone peer review.
They should not be considered conclusive, used to inform clinical practice,
or referenced by the media as validated information.

Bridging the Gap Between Microstructurally Resolved Computed Tomography-Based and Homogenised Doyle-Fuller-Newman Models for Lithium-Ion Batteries

E. C. Tredenick

eloise.tredenick@eng.ox.ac.uk

Department of Engineering Science, University of Oxford, Oxford, OX1 3PJ, UK https://orcid.org/0000-0001-9105-2858

A. M. Boyce

Electrochemical Innovation Lab, Department of Chemical Engineering, University College London, London, WC1E 7JE, UK

S. Wheeler

Department of Materials, University of Oxford, Oxford, OX1 3PH, UK

J. Li

Electrochemical Innovation Lab, Department of Chemical Engineering, University College London, London, WC1E 7JE, UK

Y. Sun

Department of Materials, University of Oxford, Oxford, OX1 3PH, UK

R. Drummond

Department of Automatic Control and Systems Engineering, University of Sheffield, Sheffield, S1 3JD, UK

S. R. Duncan

Department of Engineering Science, University of Oxford, Oxford, OX1 3PJ, UK

P. S. Grant

Department of Materials, University of Oxford, Oxford, OX1 3PH, UK

P. R. Shearing

Department of Engineering Science, University of Oxford, Oxford, OX1 3PJ, UK

Article

Keywords:

Posted Date: November 22nd, 2023

DOI: https://doi.org/10.21203/rs.3.rs-3639668/v1

License: This work is licensed under a Creative Commons Attribution 4.0 International License.
Read Full License

Additional Declarations: There is **NO** Competing Interest.

Bridging the Gap Between Microstructurally Resolved Computed Tomography-Based and Homogenised Doyle-Fuller-Newman Models for Lithium-Ion Batteries

E. C. Tredenick*[1,6], A. M. Boyce[2,3,6], S. Wheeler[4,6], J. Li[2,6], Y. Sun[4,6], R. Drummond[5], S. R. Duncan[1,6], P. S. Grant[4,6] and P. R. Shearing[1,2,6]

[1]Department of Engineering Science, University of Oxford, Oxford, OX1 3PJ, UK
[2]Electrochemical Innovation Lab, Department of Chemical Engineering, University College London, London, WC1E 7JE, UK
[3]School of Mechanical and Materials Engineering, University College Dublin, Dublin, Ireland
[4]Department of Materials, University of Oxford, Oxford, OX1 3PH, UK
[5]Department of Automatic Control and Systems Engineering, University of Sheffield, Sheffield, S1 3JD, UK
[6]The Faraday Institution, Quad One, Harwell Campus, Didcot, OX11 0RA, UK

Abstract

Lithium-ion batteries (LIB) are synonymous with the modern age of electrification, yet advances in battery design, manufacturing, and chemistry are still urgently needed. Mathematical modelling plays an important role in understanding LIB performance and can provide physics informed design directions, optimisation and explain outcomes. We present an exploration and detailed comparison of the commonly used homogenised Doyle-Fuller Newman (DFN) model and the high fidelity X-ray computed tomography (CT) based microstructural model for LIBs. We provide insights into the relative benefits of each model and highlight why they are important to battery technology development. Alongside experiments, we use the models to explore and compare two common cathode chemistries, lithium nickel manganese cobalt oxide, $Li[Ni_{0.6}Co_{0.2}Mn_{0.2}]O_2$ (NMC622), and lithium iron phosphate, $LiFePO_4$ (LFP), and investigate the influence of electrode thickness and discharge current density. The DFN and CT image-based models show good alignment for averaged LIB metrics, such as the voltage response and active material utilisation, demonstrating that homogenised, computationally inexpensive models are an essential basis for battery design and optimisation. The CT-based microstructural model provides further insight into localised particle and electrode dynamics, taking into account heterogeneities that are a source of battery degradation. Qualitatively, the models also compare well with experimental secondary ion mass spectrometry (SIMS) mapping of the Li concentration in the active particles across the electrode thickness.

As battery manufacturing continues to grow in response to the electrification of transport, the lithium-ion battery (LIB) is increasingly becoming a commoditised item. The LIB supply chain is predicted to grow by 30% annually up to 2030, reaching a market size of 4.7 TWh, compared with 0.7 TWh currently.[1] There is commercial advantage and growing pressure to be able to accelerate the cell design and optimisation process and to reduce costs. Optimising cell design quickly is challenging for cell manufacturers because new battery materials and applications emerge frequently and often unexpectedly. Delivering design optimisation to meet these challenges can only be achieved by a shift away from dependence on trial and error and move towards greater automation including the use of mathematical modelling.[2]

*Email: eloise.tredenick@eng.ox.ac.uk

Many battery models have been developed to meet the needs of cell designers.[3,4] The scope of these models is multiscale, going from the pack-level[5] all the way down to simulating individual particles[6] and molecules.[7] The simplest class of battery models are those described by equivalent circuit models, which represent the current/voltage dynamics of the battery in terms of circuit elements such as resistors and capacitors.[8–10] Due to the simplicity of these models and their computational efficiency, circuit models currently dominate applications where the value of an accurate current/voltage prediction is paramount, such as battery management systems (BMS) and pack-level modelling.[11] However, by abstracting the physics of the battery, circuit models are generally not appropriate for cell design problems.

The most simple class of physics-based models are single particle models (SPM)[12] and the many variants include those with electrolyte dynamics (SPMe),[13–15] thermal effects,[16,17] degradation,[18] and the equivalent hydraulic model.[19] The SPM/SPMe models assume that the active particle Li concentration is constant through the electrode thickness, an assumption that is not appropriate for the thick electrodes of commercial cells and during fast charging.

The benchmark model for LIB modelling is the Doyle-Fuller-Newman (DFN) framework, or pseudo-two-dimensional (P2D) model, which is a physics-based continuum model based on porous electrode theory.[14,20,21] The DFN model comprises a set of coupled partial differential equations (PDEs), including nonlinear parabolic and elliptic PDEs. The DFN model is commonly 1D through the electrode thickness, x, and pseudo 1D through the radius of the spherical particle, r, and is hence referred to as "pseudo-2D" (1 + 1D). A continuum based approach is applied to describe the electrode microstructure, which includes a description of the carbon binder domain (CBD) and the interconnected pores, and the particles are assumed to be spherical and evenly distributed through the electrode thickness. Potentials in the solid particles and liquid electrolyte are modelled, along with the Li ion concentration in the particles and liquid electrolyte, and the reaction current density. The Python implementation PyBaMM[22] uses the DFN model, building on DUALFOIL[23] code. Extensions of the DFN model have been considered recently and include multiple layers of different chemistries within the anode, cathode or both, and is termed the multilayer DFN model (M-DFN),[24] and the many particle DFN model (MP-DFN) that is able to consider an active particle size distribution.[25,26] There are homogenised 3D DFN models (3 + 3D, that use three-dimensions to describe both the electrode and the particles), that can allow for more realistic descriptions such as active particles that are not spherical, and particle cracking.[3,21] 3D microscopic, 3D homogenised and DFN-type models including active particle size distributions were compared for a 3C discharge of a $LiCoO_2$ (LCO) electrode,[26] providing important information including detailed voltage profiles. There are different modelling approaches for lithium iron phosphate, $LiFePO_4$ (LFP) including single particles that are not described by spherical diffusion, but instead phase behaviour,[6] and phase transitions using a shrinking core.[27]

Table 1: Comparison of DFN and CT scan domain models, where ε is the electrolyte volume fraction, b is the tortuosity and R is the particle radius.

	DFN model - averaged domain	CT scan domain
Experimental data validation accuracy	✓	✓
Computation Time	Seconds	Hours to days
Geometry	Additional parameters required for ε, b or R	Solved over individual particles - don't need ε, b or R as found from CT scan domain (except b for LFP).
Special domain features	-	Ability to alter phase compositions using techniques such as morphological operations. Electrode volumes can also be copied, mirrored and stacked to change electrode thickness.[28]
Dimensions	1D in x (through electrode), plus 1D (pseudo) in r (spherical particle radius), so pseudo-2D (1+1D)	3D in x, y, z, plus 3D (pseudo) through particle (of any shape), so pseudo-6D (3+3D).
X-ray CT Instrument	-	Resolution of desired geometrical features is dependent on limitations of CT instrument and morphology of the microstructure in question, e.g. inability to capture LFP CBD.
Software required	MATLAB®, Python, C++ and others	COMSOL®MultiPhysics, Simpleware ScanIP and others.
Optimisation	✓	✓Possible but involves increased computation times.

X-ray computed tomography (CT) imaging has only recently been applied to battery research

and in general CT is a relatively new tool for the electrochemical field.[4] CT image-based models are also continuum models, but they permit spatial resolution of the collection of particles that comprise a representative electrode volume. Image-based models are able to capture the realistic shape of particles accounting for their non-spherical geometry and non-uniform dispersion within the electrode volume, and both factors have been shown to play a key role in battery performance and long term degradation.[28] In some cases, given sufficient CT imaging resolution and computational resources, it is possible to resolve the microstructural details within the CBD. However, this detail is often homogenised due to the lack of CT imaging resolution or to maintain practical computation times. CT image-based models use similar equations to the P2D DFN model, but the particle size is implicit within the model, and the CBD, if resolved, is modelled as a separate electrically conductive medium. CT image-based models are resolved in 3D across the electrode thickness, including the particle in 3D, and therefore is sometimes referred to as pseudo-6D (3 + 3D). The model is created by discretising the segmented CT image to mesh elements. Since the governing electrochemical and transport equations are solved for the exact geometry, it is possible to probe the influence of local heterogeneities, such as variations in pore and particle size, shape and distribution.[4,28–30] The electrochemical descriptions can be coupled with Li intercalation or de-intercalation induced stresses in the active particles, and for example the influence of particle voids on degradation behaviour can be investigated.[31] There has been limited comparisons of image based to DFN models. There is one study[32] showing a brief comparison of voltage data for LFP electrodes with good agreement but they did not consider the full details of the CBD.

The advantages and disadvantages of the DFN and microstructural CT model are summarised in Table 1. While the CT model simulations are information-rich, the drawbacks of solving the model with high spatial resolution are the computational demand and complexity,[4] along with the need for high resolution CT scanners. For problems such as estimating the model parameters, this computational effort can be limiting.

LIB experiments commonly focus on the electrode voltage response, whereas physics-based models can reveal electrode internal processes, such as the underlying Li ion concentration profiles and spatially-resolved potential responses. Further, much of a LIB's practical performance relates to Li dynamics within the electrode. Unfortunately, spatially and chemically resolving the local Li concentrations in the active particles by experiments, such as various types of electron or other microscopies, is difficult. A promising experimental technique is plasma focused ion beam/ secondary ion mass spectrometry (PFIB/SIMS), which allows qualitative visualisation of the active particle concentration gradients at the scale of the electrode thickness, at a particular point in the charge or discharge.[4,33–37]

In this paper, we compare the homogenised modelling approach of the DFN model with the CT image-based microstructural model. These two models contain the same physics, with similar governing equations, but are resolved over different domains. Single particle (SPM and SPMe) type models that set the solid particle concentration as constant through the electrode, or equivalent circuit models, are too simple for this problem. We aim to understand the effects of non-uniform particle and electrolyte gradients through the electrode thickness, when discharging at high C rates (1C, 2C, 5C) and for relatively thick (80 μm, 90 μm and 160 μm) electrodes. We apply the models to two electrode chemistries of lithium nickel manganese cobalt oxide, $Li[Ni_{0.6}Co_{0.2}Mn_{0.2}]O_2$ (NMC622), and lithium iron phosphate, $LiFePO_4$ (LFP), to avoid chemistry-specific conclusions. The model outputs are compared to standard voltage experiments and to PFIB/SIMS based Li mapping across an LFP electrode.

Results and Discussion

Electrode Characterisation

Fig. 1 shows the particle radius histograms for the NMC622 and LFP electrodes, obtained from CT images. The NMC and LFP are positive-skewed, with the NMC distribution more positively-skewed than LFP (skewness of 0.96 and 0.79 for NMC and LFP, respectively). The total number of particles sampled is significantly higher for LFP (392 particles within a 90 μm thick electrode), compared to NMC (172 particles within a 80 μm thick electrode) because of the smaller LFP average radius of 0.4 μm compared with 4.9 μm for NMC. There are a small number of particles with radii up to three times the mean radius, especially for NMC where there are eight large particles (larger than 11 μm) including particle with radii of 14.7 μm. The relatively small LFP particle radius required a nano-CT scanner to resolve, rather than a more commonly available micro-CT scanner. The nano-CT scanner also allowed the acquisition of the CBD in the coarser length-scale NMC electrode. The average electrolyte volume fraction is 0.293 and 0.375, for NMC and LFP, respectively, obtained from CT images.

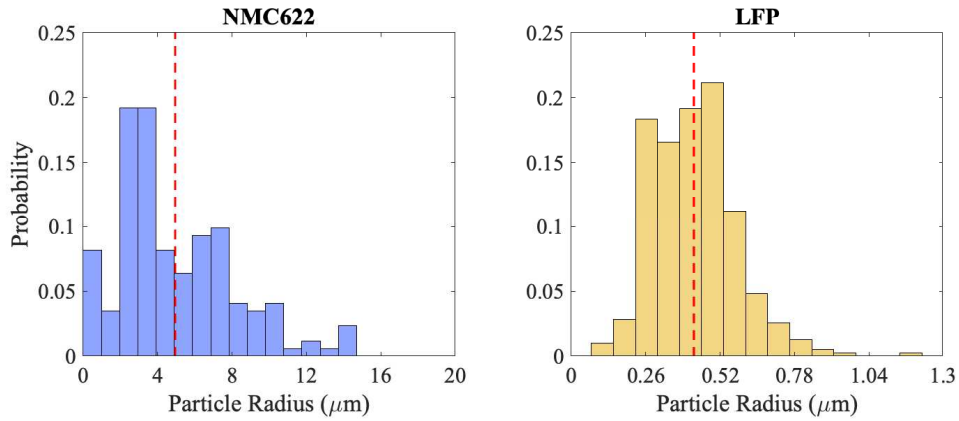

Figure 1: Histograms of the NMC622 and LFP particle radius, obtained from CT scans. The mean radius is given by the red dashed line. The mean NMC particle radius is 4.9 μm $\pm$ 3.1 μm and LFP is 0.4 μm $\pm$ 0.1 μm. There are some large particles with radii 14.7 μm and 1.2 μm for NMC and LFP, respectively.

Modelling Results

We solve the (i) homogenised Doyle-Fuller-Newman model (DFN model), and (ii) microstructurally resolved CT-based model considering the DFN equations (CT model), as described in "Methods". A total of six cases are considered: NMC at 1C and 5C, for electrode thicknesses of 80 μm and 160 μm, and LFP at 2C and 5C for a 90 μm electrode thickness. We compare the model results to experimental data for LFP, while models for NMC have been compared to experiments reported elsewhere.[24,28] The computational domains for both models are shown in Fig. 2, which also shows the different phases of active particle, carbon binder and pore space.

Fig. 3 shows the simulated voltage against capacity for NMC (A) and LFP (B). For NMC in Fig. 3 (A), the profiles compare well in terms of qualitative shape and predicted capacity, especially at 1C. For LFP in Fig. 3 (B), the profiles agree with experiment at 5C, while the agreement of the 2C profile is reduced because the experimental training data for model parametrisation was taken at 5C. The voltage response shows a sharp drop in capacity at 5C for the 160 μm thick NMC electrode, and at 5C for the 90 μm thick LFP electrode. This drop in capacity is indicative of under-utilisation of the active particles, where the normalised particle concentration has not reached unity throughout the electrode. This arises because of Li ion concentration depletion in the electrolyte and the local Li concentration tends to zero. Considering the fundamental differences between the two models, in terms of homogenised or microscopic, the voltages are encouragingly similar. The results also underline the importance of correctly specifying critical parameters and functions in both models,

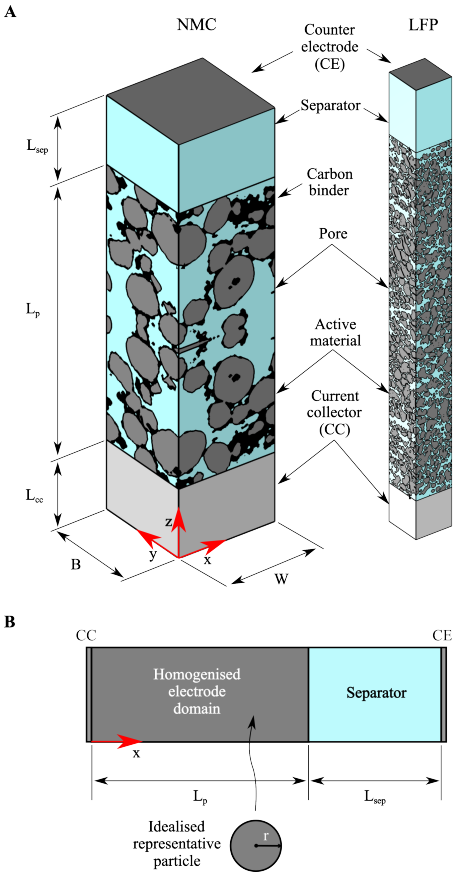

Figure 2: (A) The computational domain for the image-based CT model for NMC (L_p = 80 μm and 160 μm) and LFP (L_p = 90 μm) electrodes. L_{cc} = 10 μm and L_{sep} = 16 μm, while $B = W$ = 30 μm for NMC electrodes and $B = W$ = 10 μm for the LFP case. (B) The domain for the pseudo-2D DFN model (equations solved both through the electrode in x and in a representative idealised particle in r), where all relevant dimensions match the microstructural model in (A). The scales are different between sub-figures and is described in more detail in Fig. S1.

such as the open circuit potential (OCP) function for each chemistry, which were determined by fitting experimental results, and the OCP function is more dominant in determining voltage results than the geometric domain.[24]

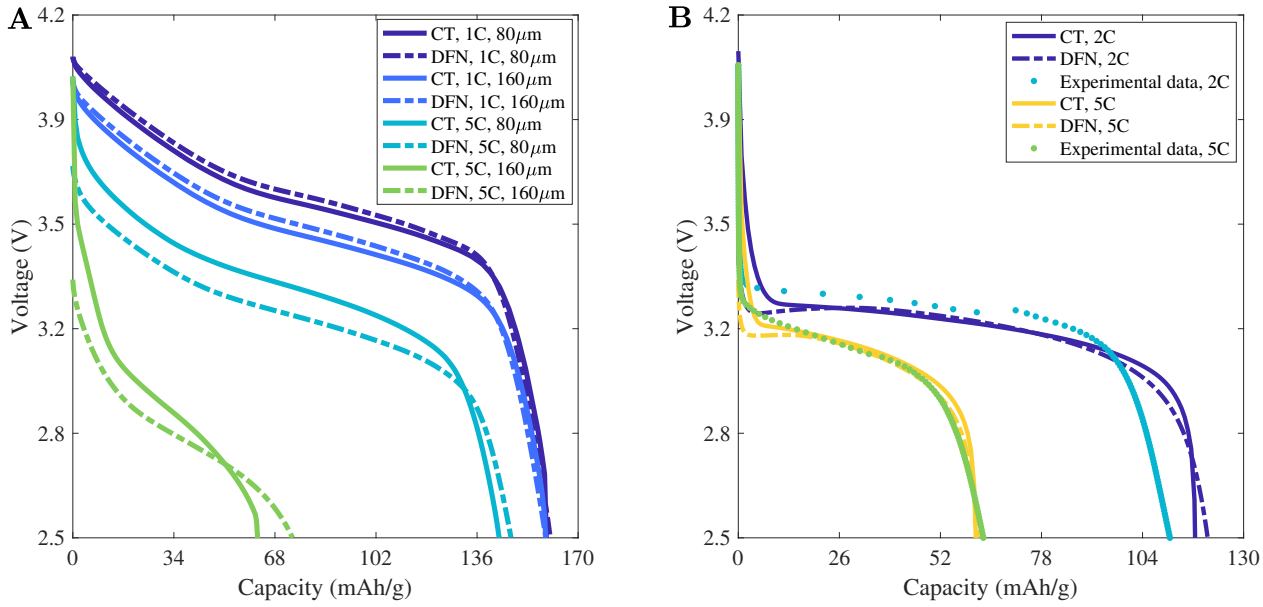

Figure 3: Voltage profiles with capacity for NMC (A) and LFP at 90 μm (B). NMC622 and LFP are characterised by specific capacities at 0.05C of 175 mAh/g and 150 mAh/g, respectively.

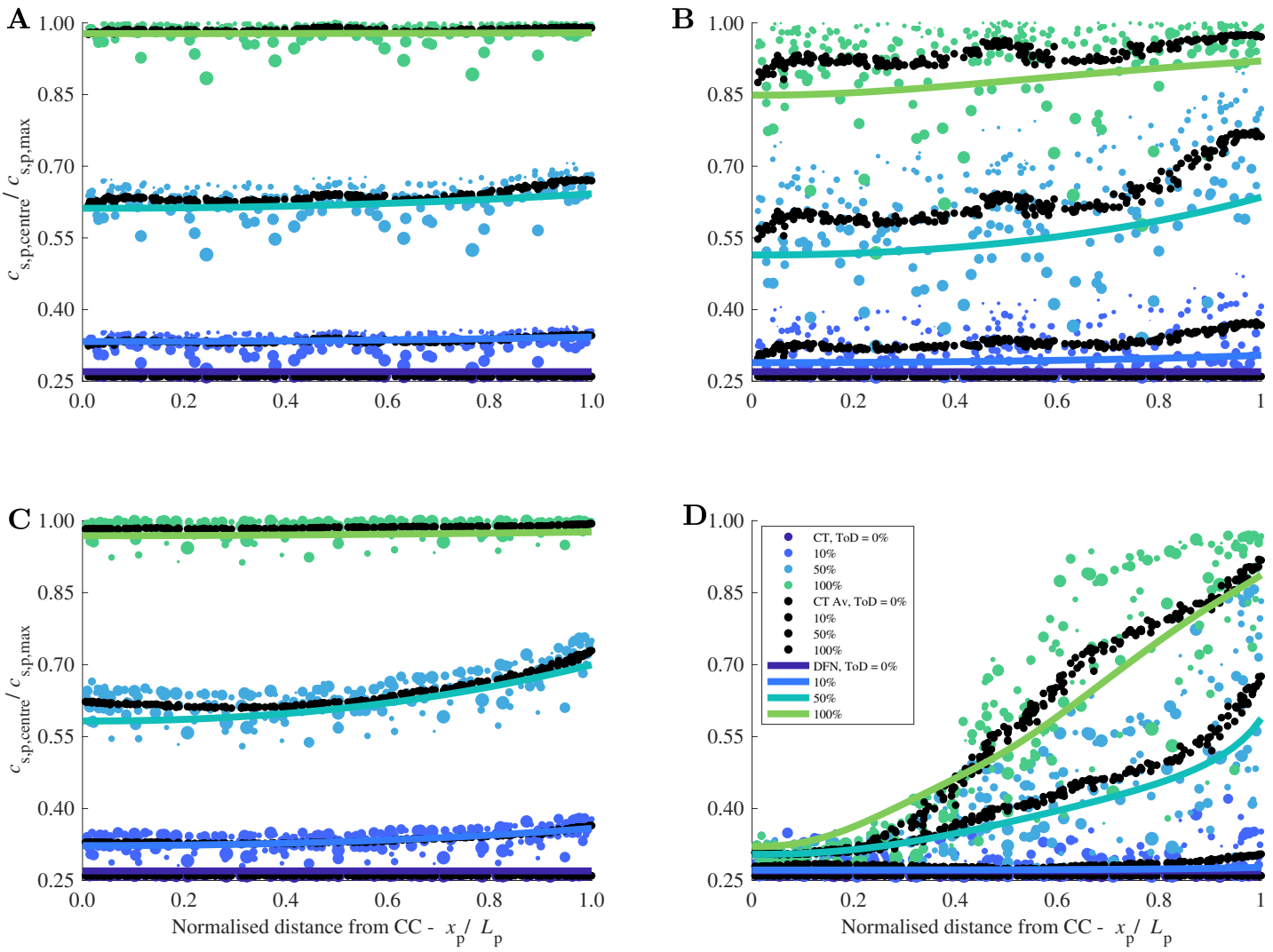

Figure 4: Simulated normalised Li concentration at the centre of NMC particles - 1C, 80 μm (A), 5C, 80 μm (B), 1C, 160 μm (C), and 5C, 160 μm (D), at range of ToD (time of discharge). The normalised Li concentration at the centre of the particle ($c_{s,p,centre}/c_{s,p,max}$) is shown as a function of distance from the current collector. 0% ToD is the start of discharge and 100% is the end. DFN model results are represented by solid lines and CT model results are represented by markers. The CT model results also indicates the particle radius shown with the marker size, along with the moving average of the concentration shown in black. The moving average is obtained from 30 (A,B) or 50 (C,D) particles. The current collector (CC) is on the left and separator on the right of each subfigure.

Figs. 4 and 5 shows the simulated Li active particle concentrations at the centre of the particle for NMC and LFP, respectively, as a function of distance through the electrode thickness, at different time of discharges (ToD). The DFN model is shown as the solid lines, while the CT results are shown as points from individual particles, where the size of the point is related to the particle radius. The moving averages of the particle concentrations for the CT model results are shown as black points. In all cases, the CT results show that, as expected, the smaller particles lithiate faster than the larger particles. For NMC in Fig. 4, there is good agreement between the DFN and CT models, particularly at 1C in (A) and (C). As the DFN model is solved using an average approach, including the mean particle radius of the CT image data, this supports the good agreement to the CT moving average as expected. At 5C in (B) and (D) the agreement is close to the moving average, but there is a larger distribution of Li concentrations produced with the CT model. At the largest electrode thickness and C rate in (D), the Li concentration profile becomes noticeably sloped, with regions close to the current collector at much lower concentration than close to the separator. The particles are not fully discharged through the thickness of the electrode and through the particle radius, which

represents significant under-utilisation of active particles related to electrolyte depletion.

For LFP in Fig. 5 and Supplementary Fig. S2, the slope of the Li profiles are markedly different with an 'S' shape or travelling front across the electrode thickness as the discharge proceeds, approximately segregating discharged and charged regions of the electrode. This distinctive shape arises from the voltage plateau in the OCP profile.[24] As seen earlier in the voltage profiles, for 5C in Fig. 5 (B), there is better agreement than at 2C (A) because the model parameters were fitted at 5C. Supplementary Fig. S3 shows the simulated state of charge (SOC) for LFP compared with the SOC estimated experimentally (calculated based on measured capacity). The modelled SOC profiles agree with one another, and with the experimental data. At 2C, the SOC changes by approximately 80% across the cycle, while at 5C the SOC changes only by 40% because of a larger extent of electrolyte depletion and active material under-utilisation.

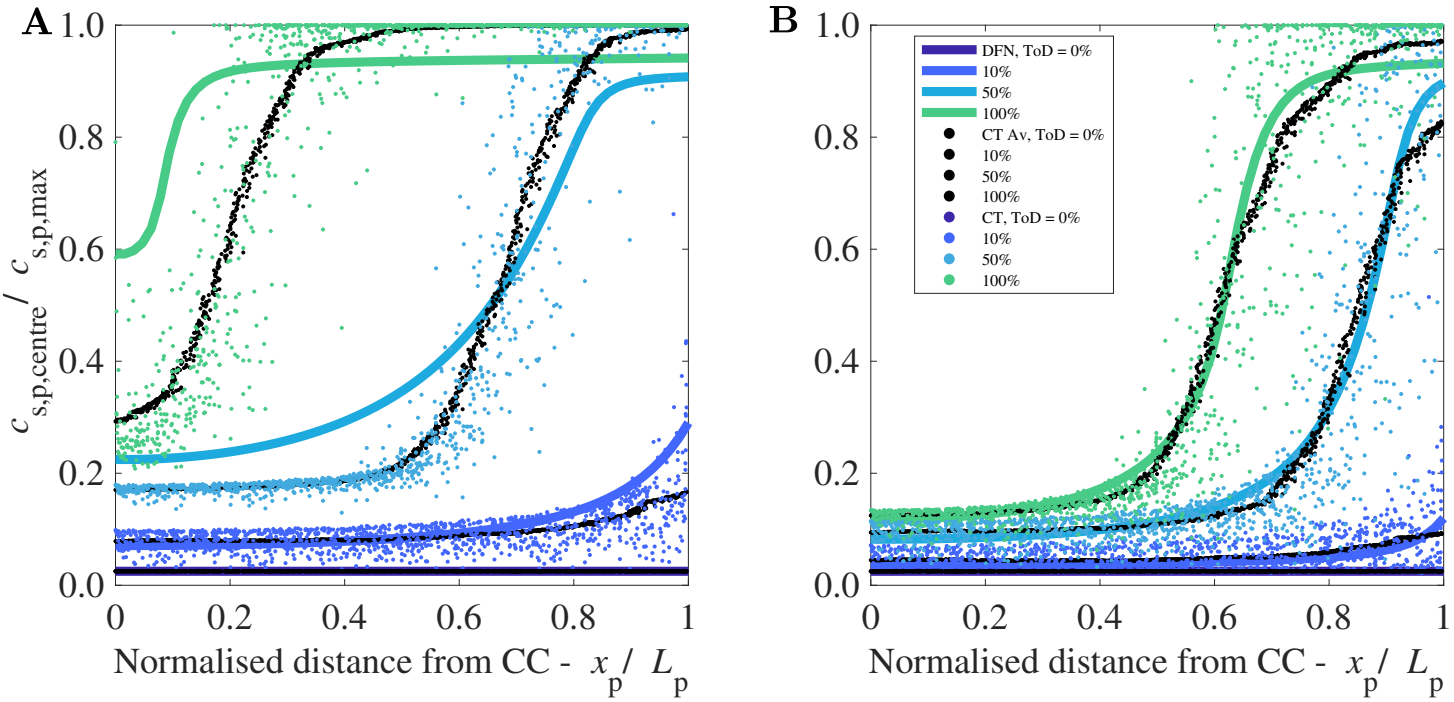

Figure 5: Simulated normalised Li concentration at the centre of LFP particles - 2C (A) and 5C (B), at range of ToD, across a 90 μm electrode. The normalised Li concentration at the centre of the particle ($c_{s,p,centre}/c_{s,p,max}$) is shown as a function of distance from the CC. 0% ToD is the start of discharge and 100% is the end. DFN model results are solid lines and CT model results are points. The CT model concentration moving average is shown in black. The moving average is obtained from 200 particles. The CC is on the left and separator on the right of each subfigure.

Fig. 6 shows the CT model results for the normalised Li concentration of the active particles for NMC (A) and LFP (B) (whereas Figs. 4 and 5 showed only the centre). The thinner 80 μm NMC electrode (A) is the only case that is fully discharged at 100% ToD, represented by a single colour throughout and indicating full lithiation. For a 90 μm thick LFP electrode (B), the active particles are close to being completely lithiated at the end of discharge but a through thickness Li gradient has developed as previously described. For the same electrode at 5C, only particles approximately half way across the electrode are significantly lithiated by the end of discharge at 100% ToD. A similar profile arises for a 160 μm thick NMC electrode (A). Supplementary Fig. S2 shows, encouragingly, for LFP that the DFN and CT models give similar Li concentrations at the active surface. The Li concentration in the centre of the particles is similar to the surface.

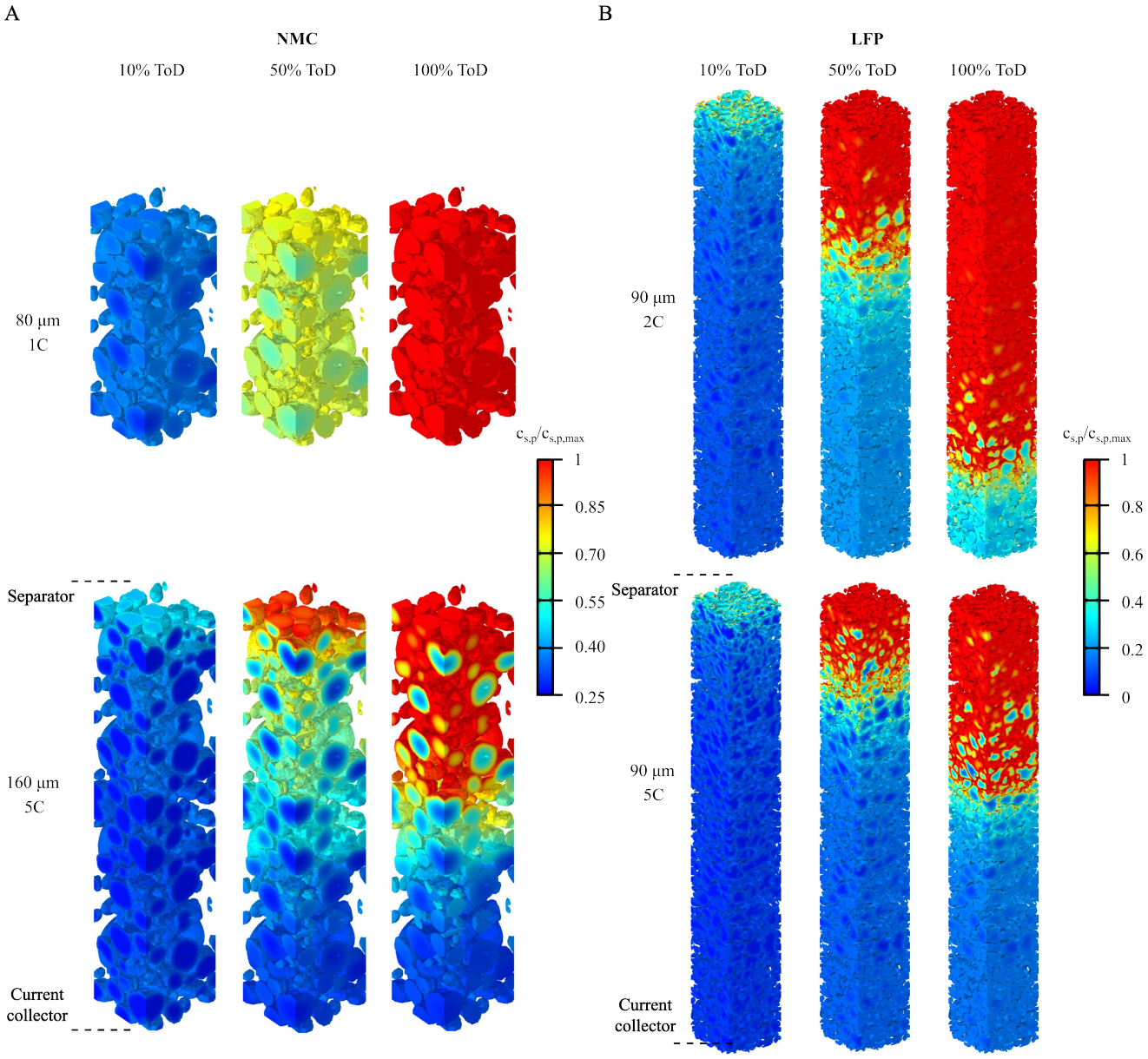

Figure 6: 3D CT model results for normalised Li concentration in the active particles ($c_{s,p}/c_{s,p,max}$) for NMC (A) and LFP (B). The figures are not the same scale.

Fig. 7 shows the simulated concentration of Li in the electrolyte through the electrode thickness for NMC and LFP as a function of discharge time. The DFN and CT results compare well over both space and time. All subfigures exhibit complete Li ion concentration depletion, except for the case of 80 μm thick NMC electrode at 1C (A). The Li concentration in the electrolyte for LFP (C,D) changes with time more significantly than NMC, whereas NMC (A,B) quickly reaches a steady-state, especially for 1C (A), where the steady-state has been reached after 10% ToD. The CT model for LFP has less range in concentrations at a particular point in the electrode and a specific ToD. For the CT model for NMC (A, B), there are a range of concentrations at a particular point in the electrode and a specific ToD, because of the wide range of particle radii and pore sizes.

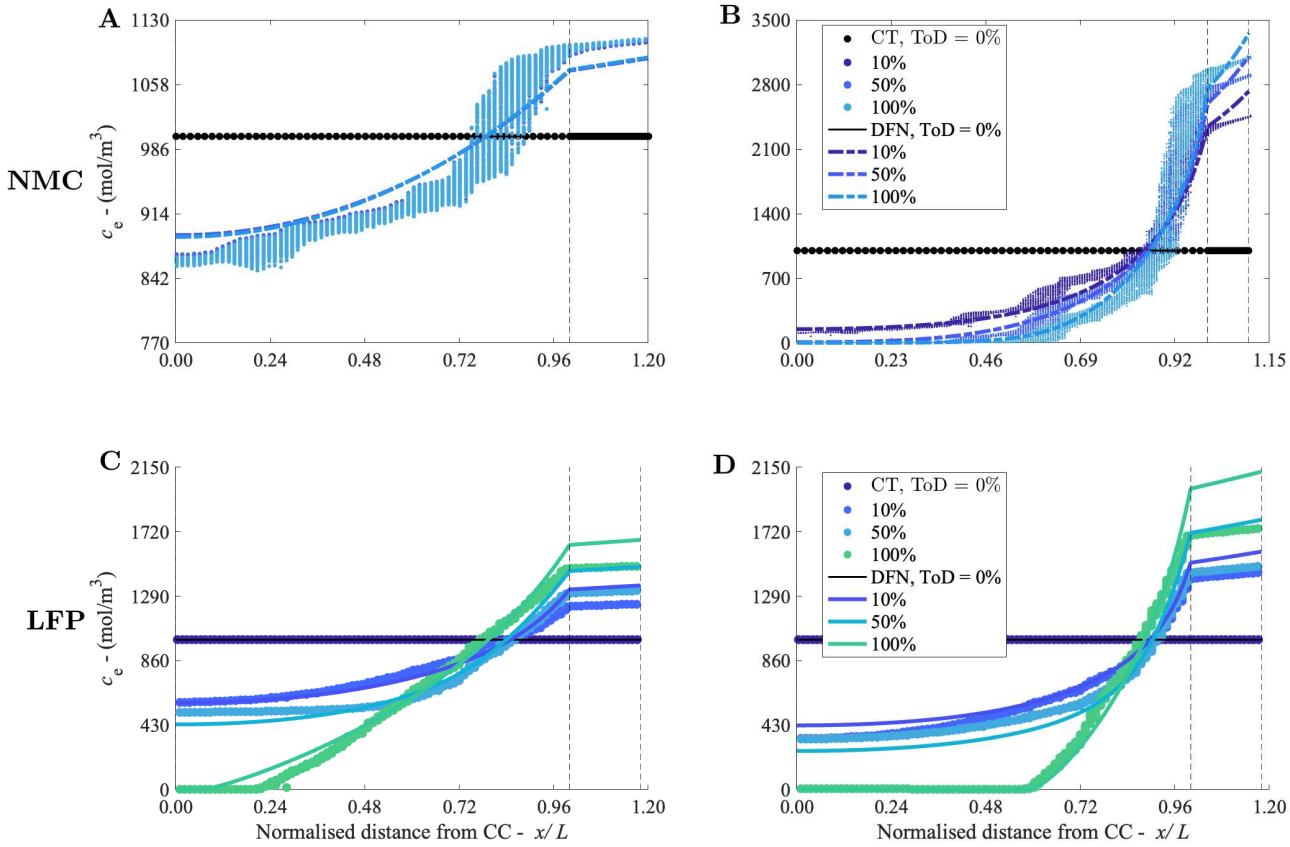

Figure 7: Simulated Li electrolyte concentration (c_e) of NMC electrodes at 1C, 80 μm (A), 5C, 160 μm (B), and LFP at 2C, 90 μm (C), 5C, 90 μm (D), at range of ToD (time of discharge). The CT model is shown as points and DFN as solid lines. The CC is on the left and separator on the right.

Fig. 8 shows a comparison of the calculated through thickness Li concentration for the CT model (A), DFN model (B) and SIMS Li mapping (C,D), for an LFP, 90 μm thick electrode at the end of a 5C discharge. The model shows the normalised Li concentration of active particles ($c_{s,p}/c_{s,p,max}$), and the SIMS concentrations are the normalised intensity of the $^7Li^+$ signal from the particles (after the electrolyte was dried in a protective atmosphere). Consistent with the 'S' shape or travelling front of the Li concentration profile for LFP described earlier (Figs. 5), there are two reasonably well delineated regions of high and low concentration, with a gradual region approximately at the centre of the electrode thickness. The regions of relatively high Li concentration near the separator are similar across the subfigures. Given that the SIMS results were not used for the model fitting (as the voltage measurements were used instead) these independent results are positive. Qualitatively, the comparison between experiment and both models is encouraging and a comparatively rare study of simulation and experiments of spatially resolved, internal Li dynamics. Using LFP as the active material is useful for this type of qualitative comparison because its open circuit potential shape with a long plateau of constant voltage leads to a distinct separation between charged and

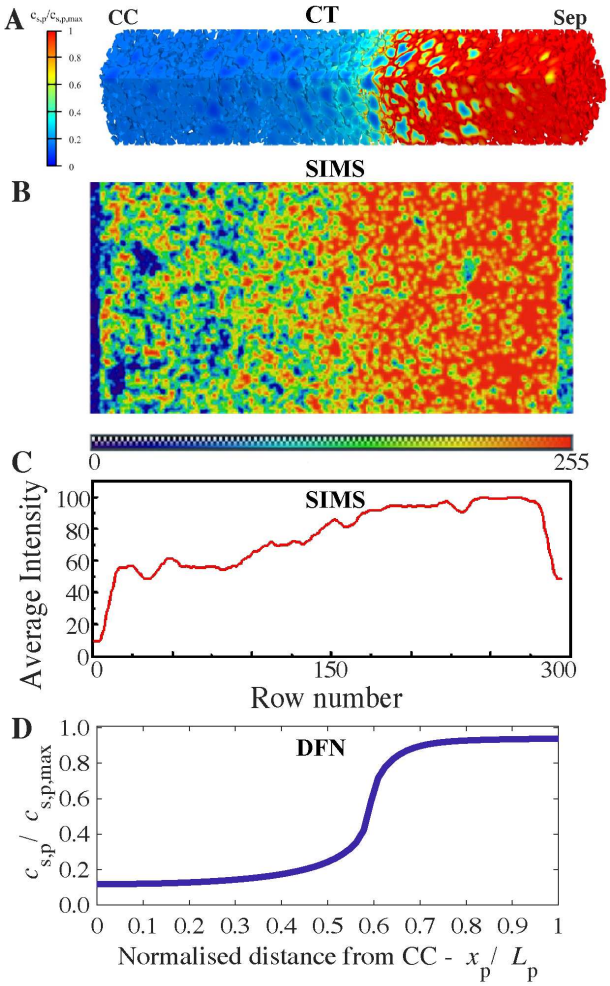

Figure 8: Li concentration of active particles for a 90 μm thick LFP electrode at 5C discharge, at the end of discharge (100% ToD). (A) and (D) are the simulated normalised Li concentration of solid particles, $c_{s,p}/c_{s,p,max}$. (B) SIMS mapping of $^7Li^+$ presented as an 8-bit colormap with pixel value ranging from 0 to 255. (C) is the normalised moving average of the Li ion intensity (n=10) from (B). (D) is the Li concentration averaged over the particle radius. The subfigures have been aligned at the ends of the electrode, with error of ± 1 μm. The results in (A) are replotted from Fig. 6 and (D) is from Supplementary Fig. S2 (C).

uncharged regions across the electrode thickness at intermediate states of charge.

Table 2: Number of fitted parameters for the DFN and CT models. $*\varepsilon_{e,p}$ is taken from the experimental results as it is calendared to 30% porosity, then fitted slightly from there.

	DFN	Total	CT	Total
NMC622	$b_p, k_p, R_c, \varepsilon_{CBD,p}$	4	k_p, σ_{CBD}	2
LFP	$\varepsilon^*_{e,p}$	1	$b_p, D_{s,p}, k_p, \varepsilon_{CBD,p}$	4

Table 2 shows the total number of parameters required to be fitted to experimental data for each model. The number of fitted parameters are generally similar, with the CT model for NMC and the DFN model for LFP having the lowest number of parameters (2 and 1, respectively). The fitting of LFP to experimental data started by (i) using the DFN model to find a baseline set of parameters, (ii) further refining using the CT model and calculating averaged parameters from the CT results, and then (iii) the DFN model adopted the parameters refined by the CT model where possible (for example the radius of the particle, R_p, carbon binder domain volume fraction, $\varepsilon_{CBD,p}$, tortuosity, b_p, and reaction rate constant, k_p). This shows the benefits of coupling a CT-image based model with a DFN model, and vice versa; using a homogenised DFN model to first find parameters as a basis for the CT model. To reduce the number of fitted parameters further, additional experiments could be undertaken, for example, to obtain directly values for internal resistance, R_c, and NMC electronic conductivity in the CBD, σ_{CBD}, LFP particle diffusivity, $D_{s,p}$, and tortuosities.[38,39]

Conclusion

The dynamic response of the LFP and NMC-based LIB electrodes has been simulated by a Doyle-Fuller-Newman and CT-based model. For the six electrode cases investigated, the relatively simple DFN model incorporates sufficient homogenised microstructural detail to agree with the detailed microstructural descriptions available in the CT model. Both models can explain experimental data suggesting they have sufficiently captured the governing mechanisms of lithium ion electrode dynamics. The CT and DFN models agree well for NMC and LFP based electrodes, in terms of voltage response, particle and electrolyte Li concentration, and state of charge. The models also agree qualitatively with the SIMS mapping of $^{7}Li^{+}$ across the thickness of an LFP-based electrode. The DFN model is useful for rapid optimisation and design of battery electrodes and reveals internal electrode dynamics such as critical spatial distributions of Li ion concentration in the electrolyte and particles. The image-based model is capable of capturing and predicting heterogeneities in electrode performance that are important in electrode degradation and operation of batteries under more demanding conditions, such as high current densities.[31,40] The DFN model requires 20 s or 50 s and 2.5 GB on a desktop computer, while the CT model requires 8 h or 15 h and 100 GB random access memory to execute on a high-performance computer, for NMC and LFP, respectively. As computing capabilities and CT-scanners continue to increase in power, resolution, availability and reduce in cost, the CT model approach can be expected to gain in popularity. We demonstrated how the DFN and CT models can interact beneficially when parametrising the models. Future work might include a 3D homogenised DFN model that could be utilised to tailor local microstructure variations, allowing simulation of non-spherical particles, as well as degradation effects including cracking and swelling.[3,21]

Methods

Mathematical Models and Parameters

Numerical Solution Procedure

The DFN model, which is described in Supplementary equations (S1) to (S7), is nondimensionalised and solved numerically, by discretising the model's PDEs using second order central differences to approximate the spatial derivatives, along with averaging of the diffusivity and conductivity functions at the control volume faces. The resulting system of ordinary differential equations is solved using "ode15s" including a mass matrix, within MATLAB® 2023a.[41] Timings for the code solutions for a 1C discharge are shown in Table 4. Parameters are shown in Table 3 and the fitting was based on the four cases for NMC-based electrodes and the LFP-based electrode at 5C, using the same parameters between the DFN and CT models where possible, and fit as a priority to the voltage data.

The CT image-based model was solved using the finite element method. Simpleware ScaniP (Mountain View, CA, USA) was used to discretise the segmented image, giving linear tetrahedral meshes with the quantity of mesh elements and degrees of freedom shown in Table 4. The electrochemical and transport equations as outlined in Supplementary equations (S8) to (S11), were solved in COMSOL®MultiPhysics (v6.1, Sweden). Time stepping was handled using 2nd order backward Euler differentiation. The CBD is explicitly resolved for NMC but not for LFP with the CT model, which is instead modelled in a homogenised DFN approach.

The parameter values (Table 3) for the reaction rates, k_{p} were fitted and align with those found elsewhere,[42,47] along with the initial concentrations in the solid particles, $c_{\mathrm{s},0}$,[48] and solid particle diffusivity for LFP, $D_{\mathrm{s,p}}$.[49] The parameters between the DFN and CT models in Table 3 are either the same or similar in most cases, and for LFP the DFN model has the same parameters as the CT model except for $\varepsilon_{\mathrm{e,p}}$. For NMC, the differences in the electronic conductivities in the solid, $\sigma_{\mathrm{s,p}}$, between the CT and DFN models are to be expected due to the CBD being defined explicitly for the

Table 3: Model parameters for NMC622 and LFP based electrodes. The 'Exp' values are measured. If the CT model parameters are different to the DFN model, it is shown in brackets. *Average particle radius was determined from the CT scan data.

Parameter	Description	Unit	NMC	LFP	Source
A	Electrode cross-sectional area	m^2	9×10^{-10}	1×10^{-10}	CT
b_p	Bruggeman tortuosity factor	-	1.5 (CT n/a)	2.3	-,CT
b_s		-	1.5	1.5	-
c_{e0}	Initial concentration of Li ions in electrolyte	mol/m^3	1,000	1,000	Exp
$c_{s,p,0}$	Initial concentration of Li ions in solid particles	mol/m^3	12,662	570	-
$c_{s,p,max}$	Maximum concentration of Li ions in solid particles	mol/m^3	48,700	22,806	[42] [43]
$D_{s,p}$	Diffusivity of Li ions in solid	m^2/s	3.995×10^{-14}	1×10^{-15}	NMC[44] , -[45]
F	Faraday constant	sA/mol	96485.332	96485.332	
g	Thermodynamic factor (equivalent to $(1+\frac{\partial \ln f}{\partial \ln c_e})$)	-	1.43	1.43	
I	Current density	A/m^2	$I = I_c/A$		
I_c	Applied current	mA	3.14×10^{-5}, 1.57×10^{-4}, 6.29×10^{-5}, 3.14×10^{-4} (1C, 5C 80 μm, 1C, 5C 160 μm)	5.56×10^{-6}, 1.38×10^{-5} (2C, 5C)	
k_p	Reaction rate constant	$m^{2.5}s^{-1}mol^{-0.5}$	7.5×10^{-12} (CT 9×10^{-12})	1.25×10^{-12}	-
L_p	Thickness	μm	80, 160	90	CT, Exp
L_s		μm	16	16	Exp
R	Universal gas constant	J/K/mol	8.314463	8.314463	[45]
R_c	Internal resistance	$\Omega\ m^2$	1.8×10^{-3} (CT n/a)	n/a	
R_p	Radius of particle	μm	4.9*	0.4*	CT
T	Constant absolute reference temperature	K	293.15 (20°C)	293.15 (20°C)	Exp
t^+	Transference number of the electrolyte	-	0.37	0.37	[46]
$\varepsilon_{CBD,p}$	Carbon binder domain volume fraction	-	0.135 (CT n/a)	0.25	-
$\varepsilon_{e,p}$	Electrolyte volume fraction	-	0.3 (CT n/a)	0.2625 (CT n/a)	-
$\varepsilon_{e,s}$		-	1 (CT n/a)	1 (CT n/a)	Exp
$\sigma_{s,p}$	Electronic conductivity in solid	S/m	5 (CT 0.17)	5	Exp
σ_{CBD}	Electronic conductivity in CBD	S/m	n/a (CT 10)	-	Exp

CT model only. For the DFN model, there was a resistance added for NMC as it is known to have higher internal resistance than LFP.[50] A function for the solid particle diffusivity, D_s, was considered but did not alter the results significantly, so was not used further.

Table 4: Timings of DFN model code in MATLAB®2023a, and CT scan model in COMSOL®MultiPhysics, for NMC (80 μm) and LFP (90 μm), both at a 1C discharge. N is the number of nodes in each particle radius, r and through thickness compartment, x, and $N = 11$ is for testing purposes only. The '*' indicates the fine mesh for plotting the article figures. The DFN model was solved on a Dell, Windows 10 desktop PC, Intel(R) Core(TM), i7-10700 CPU @ 2.9GHz, 16 GB (average practical usage 2.5 GB), random access memory (RAM), 64 bit system. The CT model was solved on a Dell, Windows 10 workstation PC, Intel(R) Xeon(R), Platinum 8260 CPU @ 2.4GHz, 64 bit, 750 GB RAM (average practical usage 100 GB), high-performance computer.

	N	States	Run time
NMC - DFN	11, 11	154	0.7 s
	27, 27	810	4.4 s
	35, 55*	2,130	20.4 s
NMC - CT	7.3×10^6	8.3×10^6	8 hr
LFP - DFN	11, 11	154	0.35 s
	27, 27	810	4.2 s
	43, 65*	3,034	49.9 s
LFP - CT	4.3×10^6	6.9×10^6	15 hr

Experiment

LFP Cell Fabrication

Electrodes were comprised LFP (MTI, USA), carbon additive (C65, Imerys, UK), and polyvinylidene fluoride binder (PVDF, Solef 5130, Solvay, UK). Active materials and carbon additive were dried overnight under vacuum and a 3wt.% PVDF in 1-Methyl-2-pyrrolidinone (NMP, Sigma) solution was then produced by stirring overnight. The electrode slurry was produced by mixing the 3wt.%

PVDF in NMP solution with the active material and carbon conductive additive using a planetary mixer (Thinky ARE-250). The solid material mass fraction ratio was 92:4:4 (active material: carbon additive: binder) for the slurry, with a solid content fraction of 40%, targeting an electronic conductivity of 5 S/m. The electrode slurry was cast onto carbon-coated aluminium foil (MTI, 18 μm total thickness) using a doctor blade and drawdown table. Dried electrode sheets were calendared to a thickness that resulted in a porosity of 30%. Electrodes disks with a diameter of 14 mm were punched from the electrode sheet before drying and bringing into an argon-filled glove box (Mbraun, $H_2O < 0.1$ ppm, $O_2 < 0.1$ ppm). Electrochemical cells are prepared in the glove box using a Li metal counter electrode, 16 μm separator (H1609, Celgard) and 1 M lithium hexafluorophosphate ($LiPF_6$) in ethylene carbonate (EC): ethyl methyl carbonate (EMC) (30:70 wt.%) with vinylene carbonate (2 wt.%) electrolyte (ELYTE). Coin cells were tested using a battery cycler (LBT21084, Arbin) in a temperature-controlled environment at 20°C. The mathematical models use the values for cell weight for NMC of 2.19×10^{-7} g, 4.38×10^{-7} g (thickness 80 μm, 160 μm), and LFP of 1.84×10^{-8} g (thickness 90 μm).

Table 5: Information for the NMC half cell

Description	Value
Specific capacity at 0.05C	175 mAh/g
Min Voltage	2.5 V
Max Voltage	4.2 V

Table 6: Information for the LFP half cell

Description	Value
Specific capacity at 0.05C	150 mAh/g
Min Voltage	2.5 V
Max Voltage	4.2 V

Computed Tomography Scan Acquisition

Both NMC and LFP microstructures were captured using lab-based nano X-ray tomography. The methodology for NMC microstructure acquisition can be found in a previous study,[28] while the LFP image was acquired as follows. A small disk-shaped electrode with a diameter of approximately 1 mm was obtained from an electrode sheet. The disk was then affixed to a pin head using a fast-setting epoxy. A micro-milling laser technique was utilised to reduce the diameter of the electrode to about 90 μm, resulting in a pillar-shaped specimen. A lab-based X-ray nano-CT system (Zeiss Xradia Ultra 810 X-ray microscope, Carl Zeiss, CA, USA) was used to scan the LFP electrode pillar. The scan was performed with an isotropic voxel size of 64 nm and a field of view of 64 μm $\times$ 64 μm. To collect 1601 sequential projections over a 180° rotation, a quasi-monochromatic X-ray beam with a Cr characteristic emission energy of 5.4 keV was used. Each projection had an exposure time of 140 s.

Secondary Ion Mass Spectrometry

A Thermo ScientificTM HeliosTM G4 plasma focused ion beam microscope (PFIB) CXe DualBeamTM system, incorporating a Hiden EQS secondary ion mass spectrometer (SIMS), was used for precise cross-sectioning and spatial mapping of Li across an LFP-based electrode cross-section. The electrode was fabricated using the method described in "LFP Cell Fabrication". Measurements of the spatially resolved $^7Li^+$ isotope intensity were carried out by application of an acceleration voltage of 30 keV, a probing current of 0.1 nA, resolution of 360 nm and a field of view of 50 μm $\times$ 105 μm.

Data Availability

The data that support the findings of this study are available from the corresponding authors upon reasonable request.

Code Availability

The DFN simulation and post-processing codes that have been used to produce the results of this study are available as open-source code by author E. C. Tredenick here (link available after acceptance) and the CT model upon reasonable request.

References

[1] McKinsey and Company, "Battery 2030: Resilient, sustainable, and circular," 2023.

[2] P. S. Grant, D. Greenwood, K. Pardikar, R. Smith, T. Entwistle, L. A. Middlemiss, G. Murray, S. A. Cussen, M. J. Lain, M. J. Capener, M. Copley, C. D. Reynolds, S. D. Hare, M. J. H. Simmons, E. Kendrick, S. P. Zankowski, S. Wheeler, P. Zhu, P. R. Slater, Y. S. Zhang, A. R. T. Morrison, W. Dawson, J. Li, P. R. Shearing, D. J. L. Brett, G. Matthews, R. Ge, R. Drummond, E. C. Tredenick, C. Cheng, S. R. Duncan, A. M. Boyce, M. Faraji-Niri, J. Marco, L. A. Roman-Ramirez, C. Harper, P. Blackmore, T. Shelley, A. Mohsseni, and D. J. Cumming, "Roadmap on Li-ion battery manufacturing research," vol. 4, p. 042006, nov 2022.

[3] F. B. Planella, W. Ai, A. Boyce, A. Ghosh, I. Korotkin, S. Sahu, V. Sulzer, R. Timms, T. Tranter, M. Zyskin, S. J. Cooper, J. S. Edge, J. M. Foster, M. Marinescu, B. Wu, and G. Richardson, "A continuum of physics-based lithium-ion battery models reviewed," *Progress in Energy*, 2022.

[4] J. Scharf, M. Chouchane, D. P. Finegan, B. Lu, C. Redquest, M.-c. Kim, W. Yao, A. A. Franco, D. Gostovic, Z. Liu, *et al.*, "Bridging nano-and microscale X-ray tomography for battery research by leveraging artificial intelligence," *Nature Nanotechnology*, vol. 17, no. 5, pp. 446–459, 2022.

[5] J. M. Reniers and D. A. Howey, "Digital twin of a MWh-scale grid battery system for efficiency and degradation analysis," *Applied Energy*, vol. 336, p. 120774, 2023.

[6] M. Z. Bazant, "Theory of chemical kinetics and charge transfer based on nonequilibrium thermodynamics," *Accounts of chemical research*, vol. 46, no. 5, pp. 1144–1160, 2013.

[7] L. M. Morgan, M. P. Mercer, A. Bhandari, C. Peng, M. M. Islam, H. Yang, J. Holland, S. W. Coles, R. Sharpe, A. Walsh, *et al.*, "Pushing the boundaries of lithium battery research with atomistic modelling on different scales," *Progress in Energy*, vol. 4, no. 1, p. 012002, 2021.

[8] S. Nejad, D. Gladwin, and D. Stone, "A systematic review of lumped-parameter equivalent circuit models for real-time estimation of lithium-ion battery states," *Journal of Power Sources*, vol. 316, pp. 183–196, 2016.

[9] X. Hu, S. Li, and H. Peng, "A comparative study of equivalent circuit models for Li-ion batteries," *Journal of Power Sources*, vol. 198, pp. 359–367, 2012.

[10] G. L. Plett, *Battery management systems, Volume II: Equivalent-circuit methods*. Artech House, 2015.

[11] T. Tranter, R. Timms, V. Sulzer, F. Planella, G. Wiggins, S. Karra, P. Agarwal, S. Chopra, S. Allu, P. Shearing, *et al.*, "liionpack: A python package for simulating packs of batteries with pybamm," *Journal of Open Source Software*, vol. 7, no. 70, 2022.

[12] S. Atlung, K. West, and T. Jacobsen, "Dynamic aspects of solid solution cathodes for electrochemical power sources," *Journal of The Electrochemical Society*, vol. 126, no. 8, p. 1311, 1979.

[13] S. J. Moura, F. B. Argomedo, R. Klein, A. Mirtabatabaei, and M. Krstic, "Battery state estimation for a single particle model with electrolyte dynamics," *IEEE Transactions on Control Systems Technology*, vol. 25, no. 2, pp. 453–468, 2016.

[14] S. G. Marquis, V. Sulzer, R. Timms, C. P. Please, and S. J. Chapman, "An asymptotic derivation of a single particle model with electrolyte," *J Elect Soc*, vol. 166, no. 15, pp. A3693–A3706, 2019.

[15] G. Richardson, I. Korotkin, R. Ranom, M. Castle, and J. M. Foster *Elect Acta*, vol. 339, 4 2020.

[16] M. Guo, G. Sikha, and R. E. White, "Single-particle model for a lithium-ion cell: Thermal behavior," *Journal of The Electrochemical Society*, vol. 158, no. 2, p. A122, 2010.

[17] G. Ning and B. N. Popov, "Cycle life modeling of lithium-ion batteries," *Journal of The Electrochemical Society*, vol. 151, no. 10, p. A1584, 2004.

[18] J. M. Reniers, G. Mulder, and D. A. Howey, "Review and performance comparison of mechanical-chemical degradation models for lithium-ion batteries," *Journal of The Electrochemical Society*, vol. 166, no. 14, pp. A3189–A3200, 2019.

[19] L. D. Couto, J. Schorsch, N. Job, A. Léonard, and M. Kinnaert, "State of health estimation for lithium ion batteries based on an equivalent-hydraulic model: An iron phosphate application," *Journal of Energy Storage*, vol. 21, pp. 259–271, 2019.

[20] M. Doyle, T. F. Fuller, and J. Newman, "Modeling of galvanostatic charge and discharge of the lithium/polymer/insertion cell," *Journal of the Electrochemical society*, vol. 140, no. 6, p. 1526, 1993.

[21] H. Arunachalam and S. Onori, "What if the Doyle-Fuller-Newman model fails? A new macroscale modeling framework," in *2018 IEEE Conference on Decision and Control (CDC)*, pp. 5702–5707, IEEE, 2018.

[22] V. Sulzer, S. G. Marquis, R. Timms, M. Robinson, and S. J. Chapman, "Python battery mathematical modelling (PyBaMM)," *Journal of Open Research Software*, vol. 9, no. 1, 2021.

[23] J. Newman, "DualFoil FORTRAN Programs for the Simulation of Electrochemical Systems.," 1998.

[24] E. C. Tredenick, S. Wheeler, R. Drummond, S. R. Duncan, and P. S. Grant, "A multilayer Doyle-Fuller-Newman model (M-DFN) to optimise the rate performance of bi-layer cathodes for Li-ion batteries," 2023.

[25] T. L. Kirk, J. Evans, C. P. Please, and S. J. Chapman, "Modeling electrode heterogeneity in lithium-ion batteries: unimodal and bimodal particle-size distributions," *SIAM Journal on Applied Mathematics*, vol. 82, no. 2, pp. 625–653, 2022.

[26] A. Schmidt, E. Ramani, T. Carraro, J. Joos, A. Weber, M. Kamlah, and E. Ivers-Tiffée, "Understanding deviations between spatially resolved and homogenized cathode models of lithium-ion batteries," *Energy Technology*, vol. 9, no. 6, p. 2000881, 2021.

[27] S. Dargaville and T. W. Farrell, "Predicting active material utilization in LiFePO4 electrodes using a multiscale mathematical model," *Journal of the Electrochemical Society*, vol. 157, no. 7, p. A830, 2010.

[28] A. M. Boyce, X. Lu, D. J. Brett, and P. R. Shearing, "Exploring the influence of porosity and thickness on lithium-ion battery electrodes using an image-based model," *Journal of Power Sources*, vol. 542, p. 231779, 2022.

[29] X. Lu, A. Bertei, D. P. Finegan, C. Tan, S. R. Daemi, J. S. Weaving, K. B. O'Regan, T. M. Heenan, G. Hinds, E. Kendrick, *et al.*, "3d microstructure design of lithium-ion battery electrodes assisted by x-ray nano-computed tomography and modelling," *Nature Communications*, vol. 11, no. 1, p. 2079, 2020.

[30] J. Lin, S. Zhao, T. G. Tranter, Z. Zhang, F. Peng, D. Brett, R. Jervis, and P. R. Shearing, "Modelling and experimental investigation of Nb2O5 as a high-rate battery anode material," *Electrochimica Acta*, vol. 443, p. 141983, 2023.

[31] A. M. Boyce, E. Martínez-Pañeda, A. Wade, Y. S. Zhang, J. J. Bailey, T. M. Heenan, D. J. Brett, and P. R. Shearing, "Cracking predictions of lithium-ion battery electrodes by X-ray computed tomography and modelling," *Journal of Power Sources*, vol. 526, p. 231119, 2022.

[32] A. G. Kashkooli, S. Farhad, D. U. Lee, K. Feng, S. Litster, S. K. Babu, L. Zhu, and Z. Chen, "Multiscale modeling of lithium-ion battery electrodes based on nano-scale X-ray computed tomography," *Journal of Power Sources*, vol. 307, pp. 496–509, 3 2016.

[33] T. Sui, B. Song, J. Dluhos, L. Lu, and A. M. Korsunsky, "Nanoscale chemical mapping of Li-ion battery cathode material by FIB-SEM and TOF-SIMS multi-modal microscopy," *Nano Energy*, vol. 17, pp. 254–260, 2015.

[34] H. Masuda, N. Ishida, Y. Ogata, D. Ito, and D. Fujita, "In situ visualization of Li concentration in all-solid-state lithium ion batteries using time-of-flight secondary ion mass spectrometry," *Journal of Power Sources*, vol. 400, pp. 527–532, 2018.

[35] Y. Yamagishi, H. Morita, Y. Nomura, and E. Igaki, "Visualizing lithium distribution and degradation of composite electrodes in sulfide-based all-solid-state batteries using operando time-of-flight secondary ion mass spectrometry," *ACS Applied Materials & Interfaces*, vol. 13, no. 1, pp. 580–586, 2020.

[36] H. Xu, J. Zhu, D. P. Finegan, H. Zhao, X. Lu, W. Li, N. Hoffman, A. Bertei, P. Shearing, and M. Z. Bazant, "Guiding the design of heterogeneous electrode microstructures for Li-ion batteries: microscopic imaging, predictive modeling, and machine learning," *Advanced Energy Materials*, vol. 11, no. 19, p. 2003908, 2021.

[37] R. Franke-Lang, A. Hilger, I. Manke, S. Zavareh, M. F. Bekheet, A. Gurlo, and J. Kowal, "3D Multiscale Lithium-Ion Cell Modeling for LiFePO4 Freeze-Casted Electrode Structures Using Synchrotron X-Ray and FIB/SEM Tomography," *Advanced Theory and Simulations*, p. 2300372, 2023.

[38] F. L. Usseglio-Viretta, D. P. Finegan, A. Colclasure, T. M. Heenan, D. Abraham, P. Shearing, and K. Smith, "Quantitative relationships between pore tortuosity, pore topology, and solid particle morphology using a novel discrete particle size algorithm," *Journal of The Electrochemical Society*, vol. 167, no. 10, p. 100513, 2020.

[39] F. L. E. Usseglio-Viretta, A. Colclasure, A. N. Mistry, K. P. Y. Claver, F. Pouraghajan, D. P. Finegan, T. M. M. Heenan, D. Abraham, P. P. Mukherjee, D. Wheeler, P. Shearing, S. J. Cooper, and K. Smith, "Resolving the Discrepancy in Tortuosity Factor Estimation for Li-Ion Battery Electrodes through Micro-Macro Modeling and Experiment," *Journal of The Electrochemical Society*, vol. 165, pp. A3403–A3426, 2018.

[40] O. O. Taiwo, M. Loveridge, S. D. Beattie, D. P. Finegan, R. Bhagat, D. J. Brett, and P. R. Shearing, "Investigation of cycling-induced microstructural degradation in silicon-based electrodes in lithium-ion batteries using x-ray nanotomography," *Electrochimica acta*, vol. 253, pp. 85–92, 2017.

[41] T. M. Inc., "Matlab version: 9.14.0 (r2023a)," 2023.

[42] R. Xu, Y. Yang, F. Yin, P. Liu, P. Cloetens, Y. Liu, F. Lin, and K. Zhao, "Heterogeneous damage in Li-ion batteries: Experimental analysis and theoretical modeling," *Journal of the Mechanics and Physics of Solids*, vol. 129, pp. 160–183, 2019.

[43] A. Jokar, M. Désilets, M. Lacroix, and K. Zaghib, "Mesoscopic modeling and parameter estimation of a lithium-ion battery based on LiFePO4/graphite," *Journal of Power Sources*, vol. 379, pp. 84–90, 2018.

[44] H. Noh, S. Youn, C. S. Yoon, and Y. Sun, "Comparison of the structural and electrochemical properties of layered Li [NixCoyMnz] O2 (x= 1/3, 0.5, 0.6, 0.7, 0.8 and 0.85) cathode material for lithium-ion batteries," *Journal of power sources*, vol. 233, pp. 121–130, 2013.

[45] D. B. Newell, E. Tiesinga, *et al.*, "The international system of units (SI)," *NIST Special Publication*, vol. 330, pp. 1–138, 2019.

[46] L. O. Valøen and J. N. Reimers, "Transport Properties of LiPF6-Based Li-Ion Battery Electrolytes," *Journal of The Electrochemical Society*, vol. 152, p. A882, 2005.

[47] M. Farkhondeh, M. Safari, M. Pritzker, M. Fowler, T. Han, J. Wang, and C. Delacourt, "Full-range simulation of a commercial LiFePO4 electrode accounting for bulk and surface effects: A comparative analysis," *Journal of The Electrochemical Society*, vol. 161, no. 3, p. A201, 2013.

[48] I. Korotkin, S. Sahu, S. E. O'Kane, G. Richardson, and J. M. Foster, "DandeLiion v1: An extremely fast solver for the Newman model of lithium-ion battery (dis) charge," *Journal of The Electrochemical Society*, vol. 168, no. 6, p. 060544, 2021.

[49] C. Gao, J. Zhou, G. Liu, and L. Wang, "Lithium-ions diffusion kinetic in LiFePO4/carbon nanoparticles synthesized by microwave plasma chemical vapor deposition for lithium-ion batteries," *Applied Surface Science*, vol. 433, pp. 35–44, 2018.

[50] B. Diouf and R. Pode, "Potential of lithium-ion batteries in renewable energy," *Renewable Energy*, vol. 76, pp. 375–380, 2015.

Acknowledgements

The authors acknowledge funding provided by the Faraday Institution for project NEXTRODE (Grant number: FIRG015 and FIRG066). RD acknowledges funding by a UKIC Research Fellowship from the Royal Academy of Engineering. PRS acknowledges funding from The Royal Academy of Engineering (CiET1718/59). YS acknowledges the use of characterisation facilities and valuable discussion within the David Cockayne Centre for Electron Microscopy, Department of Materials, University of Oxford, alongside financial support provided by the Henry Royce Institute (Grant ref EP/R010145/1) and a David Cockayne Fellowship at Linacre College, University of Oxford.

Author contributions

ECT is responsible for project management, article writing, DFN model adaptation, DFN computational code creation, results, analysis, article editing and revision. AMB is responsible for article writing, CT scan model adaptation, CT computational code creation, results, analysis, article editing and revision. SW is responsible for experimental data collection for LFP, article writing and reviewing. JL is responsible for experimental data collection for CT scans, and article writing and reviewing. YS is responsible for PFIB and SIMS data collection and analysis, article editing and revision. RD is responsible for model adaptation, article writing, analysis, article editing and revision. SRD, PSG and PRS are responsible for supervision, analysis, article editing and revision.

Competing Interests

The authors declare no competing interests.

Additional information

Supplementary Information accompanies this paper.

Supplementary Files

This is a list of supplementary files associated with this preprint. Click to download.

- SI.pdf